



A low operating temperature and high performance sensor for H₂S detection based on α -Fe₂O₃/TiO₂ heterojunction nanoparticles composite

Zhiwu Xu¹ · Haixin Liu¹ · Xin Tong^{1,2} · Wenhao Shen¹ · Xiaoquan Chen¹ · Jean-Francis Bloch³

Received: 20 February 2019 / Accepted: 31 May 2019 / Published online: 4 June 2019
© Springer Science+Business Media, LLC, part of Springer Nature 2019

Abstract

Firstly, a low operating temperature and high performance sensor for H₂S detection based on α -Fe₂O₃/TiO₂ heterojunction nanoparticles (NPs) was developed by a liquid phase reaction with low synthesis temperature. Secondly, the microstructures and chemical compositions of the gas sensing material were analyzed by X-ray diffraction, scanning electron microscopy, transmission electron microscope, energy dispersive spectrometer and X-ray photoelectron spectra methods. Thirdly, with the 50 mol% α -Fe₂O₃ doping amount and operating temperature of 120 °C, the gas sensing performances of the developed α -Fe₂O₃/TiO₂ NPs composite sensor to H₂S were obtained: the responses of 3.4–15.6 to 1–50 ppm H₂S, a linear relationship between the sensor response and the H₂S concentration, the acceptable response/recovery time of 25 s and 48 s to 50 ppm H₂S, excellent selectivity (10 times higher than those of the other tested gases) to H₂S, and good repeatability and stability in 1-month duration. These excellent H₂S gas sensing performances were attributed to the effects of n–n heterojunctions of two metal oxides, which were discussed in detail. Finally, the superior performances of the developed α -Fe₂O₃/TiO₂ NPs composite sensor were compared with the other reported H₂S sensors, which the low operating temperature of 120 °C was highlighted.

1 Introduction

Hydrogen sulfide (H₂S) is a colorless, highly toxic, flammable, and corrosive gas [1]. It is one of the major toxic pollutants in oil drilling sites, natural gas processing plants, petroleum refineries, mine shafts, paper mills, and sewage treatment [2]. Moreover, according to our previous analysis results of gaseous pollutants in several pulp and paper mills [3], it was revealed that the concentrations of H₂S in the ambient air of paper mills mainly varied in the range of 1–50 ppm, which was a serious threat to human health and

environment. Therefore, from a safety point of view, it is essential to develop H₂S gas sensor for monitoring H₂S in various industrial areas.

Recently, the gas sensors based on various Metal Oxide Semiconductors (MOS) have been used for monitoring different gases due to their low power consumption, high sensitivity, low production cost, and stability [4, 5]. And therein, the reported MOS sensors detecting H₂S gas, involved SnO₂ [6], NiO [7], ZnO [8], Fe₂O₃ [9], WO₃ [10], and TiO₂ [11].

Being a significant n-type oxide semiconductor ($E_g=3.2$ eV), titanium dioxide (TiO₂) has been recognized as a potential material applied to gas sensing [12–14], due to its stability, corrosion resistance, harmlessness to human body, and high catalytic properties. However, the high operating temperature at 200–300 °C has caused both high energy consumption and short sensor life [1, 15], which limited their applications [16]. Therefore, some improved methods including composites [17, 18] and heterostructure formation [19, 20] have been employed. Over the years, some researches using cheap metal oxides as dopants have decreased the operating temperature and improved the stability, gas selectivity, and sensitivity of gas sensor. Being a common n-type semiconductor ($E_g=2.1$ eV) and a kind of

✉ Wenhao Shen
ppwhshen@scut.edu.cn

¹ State Key Laboratory of Pulp and Paper Engineering, South China University of Technology, Guangzhou 510640, People's Republic of China

² State Key Laboratory of Electronic Thin Films and Integrated Devices, University of Electronic Science and Technology of China, Chengdu 610054, People's Republic of China

³ Department of Paper, Print Media, and Biomaterials, Grenoble Institute of Technology, Univ. Grenoble Alpes, 3SR/CNRS, 38000 Grenoble, France

abundant, corrosion resistant, and environmentally friendly metal oxide [21–24], hematite ($\alpha\text{-Fe}_2\text{O}_3$) can be applied as a stable TiO_2 nanoparticles (NPs) dopant: its modification on TiO_2 NPs may form n–n heterojunction [25] that has some excellent electrochemical properties, and could improve the gas sensitivity of TiO_2 NPs accordingly [26]. Kheel et al. reported the TiO_2 -decorated $\alpha\text{-Fe}_2\text{O}_3$ nanorod sensor, although the sensor showed the good response to H_2S , it had a high operating temperature of 300 °C [5].

In this paper, to decrease the operating temperature of gas sensor, we prepared a H_2S gas sensor based on $\alpha\text{-Fe}_2\text{O}_3/\text{TiO}_2$ heterojunction NPs composite, which possessed high sensitivity, selectivity, and low operating temperature. Firstly, anatase TiO_2 and $\alpha\text{-Fe}_2\text{O}_3$ NPs were prepared by a liquid phase process with low synthesis temperature and a boiling reflux hydrolysis method, respectively. And then, using an ultrasonic method, TiO_2 was modified with different mixing molar ratios of $\alpha\text{-Fe}_2\text{O}_3$. The gas sensing performances of the developed H_2S gas sensors based on pure TiO_2 , pure $\alpha\text{-Fe}_2\text{O}_3$, and $\alpha\text{-Fe}_2\text{O}_3/\text{TiO}_2$ NPs composites were investigated, and the mechanisms of the H_2S gas sensor were further studied. Finally, compared with the other reported H_2S gas sensors prepared by MOS materials, the improved characteristics of the $\alpha\text{-Fe}_2\text{O}_3/\text{TiO}_2$ NPs composite sensor were revealed.

2 Materials and methods

2.1 Preparation of $\alpha\text{-Fe}_2\text{O}_3$ NPs

The preparation process of $\alpha\text{-Fe}_2\text{O}_3$ NPs by the boiling reflux hydrolysis method was as follows: (1) 12.121 g ferric nitrate nonahydrate ($\text{Fe}(\text{NO}_3)_3 \cdot 9\text{H}_2\text{O}$) was dispersed in 300 mL deionized water to prepare a 0.1 mol/L $\text{Fe}(\text{NO}_3)_3$ solution. The resultant solution was added into a 1 L flask and subsequently heated in an oil bath at a temperature between 80 and 90 °C. (2) Then 3.997 g caustic soda (NaOH) was dispersed in 100 mL deionized water to prepare one 1 mol/L NaOH solution and heated to boiling. It was then quickly added to the heated $\text{Fe}(\text{NO}_3)_3$ solution and stirred at 700 r/min for 10 min. (3) Similarly, 2.120 g sodium carbonate (Na_2CO_3) was dispersed in 100 mL deionized water to prepare a 0.2 mol/L Na_2CO_3 solution and heated to boiling. It was then quickly added to the heated $\text{Fe}(\text{NO}_3)_3$ solution and stirred at 700 r/min for 10 min. (4) Subsequently, the mixture was centrifuged to obtain brown $\text{Fe}(\text{OH})_3$. The excess nitrate was removed for three times by centrifugal washing with deionized water. (5) The washed $\text{Fe}(\text{OH})_3$ was dispersed in 300 mL deionized water with a 500 mL beaker, and 0.4 g ferrous nitrate ($\text{Fe}(\text{NO}_3)_2$) dissolved in 10 mL deionized water was added. (6) The pH value of the solution was adjusted to

5 with diluted nitric acid. (7) Finally, $\alpha\text{-Fe}_2\text{O}_3$ colloid was obtained by heating to boiling reflux in an oil bath for 8 h.

2.2 Synthesis of $\alpha\text{-Fe}_2\text{O}_3/\text{TiO}_2$ NPs composites

Anatase TiO_2 NPs were prepared by low temperature liquid phase process [27], which was described briefly as follows: 40 mL tetrabutyl titanate and 40 mL acetic anhydride were mixed in 100 mL cyclohexane solvent, followed by heating at 70 °C for 1 h. The resultant precipitate was centrifuged and washed with ethanol and distilled water for three times respectively, then the titanyl organic compound was obtained after being dried in air. Finally, the titanyl organic compound was added into 500 mL distilled water, and the white anatase TiO_2 colloid was obtained via heating and stirring.

In the TiO_2 colloids, different molar ratios of $\alpha\text{-Fe}_2\text{O}_3$ (10, 30, 50, 70, and 90 mol%) were added and mixed ultrasonically for 10 min [28], subsequently, the mixtures were annealed in a muffle furnace for 2 h at 450 °C with a heating rate of 5 °C/min. Therefore, the different $\alpha\text{-Fe}_2\text{O}_3/\text{TiO}_2$ NPs composites were synthesized with various doping amounts of $\alpha\text{-Fe}_2\text{O}_3$.

2.3 Characterization

The crystal morphologies and phase constitutions of both the pure TiO_2 and $\alpha\text{-Fe}_2\text{O}_3$, and their NPs composites were confirmed by X-ray diffraction (XRD) patterns with a diffractometer (PANalytical, X'pert powder) using $\text{Cu K}\alpha$ radiation of 1.5418 Å. The data were acquired with a step length of 0.013° and a step time of 15 s in a 2θ range of 20°–80°. The morphologies of the materials were examined by scanning electron microscopy (SEM, Merlin, ZEISS, Germany, 5 kV) and transmission electron microscope (TEM, JEM-2100F, Japan, 200 kV). Besides, high resolution TEM (HRTEM) was employed to investigate the internal structure of the two pure metal oxides. A scanning transmission electron microscopy (STEM)–EDS-mapping was used to check the uniform distribution of the two metal oxides in $\alpha\text{-Fe}_2\text{O}_3/\text{TiO}_2$ film. X-ray photoelectron spectra (XPS, Kratos Axis Ultra DLD) measurements with $\text{Al K}\alpha$ source were performed to further study the phase composition and structure of the samples.

2.4 Fabrication and measurements of gas sensor

The fabrication process of the H_2S gas sensor based on pure materials and $\alpha\text{-Fe}_2\text{O}_3/\text{TiO}_2$ NPs composites could be divided into four steps: (1) Seven alumina plate substrates were put into a 50 mL beaker and ultrasonically cleaned for 10 min with acetone, ethanol, and distilled water, respectively and orderly. As described in Sect. 2.2, seven solutions, pure TiO_2 , 10, 30, 50, 70, 90 mol% $\alpha\text{-Fe}_2\text{O}_3/\text{TiO}_2$ and pure $\alpha\text{-Fe}_2\text{O}_3$, were prepared respectively. (2)

After mixing 10 mL of the seven solutions and 1 mL terpinenol separately, the mixtures were dripped onto the surfaces of the plate substrates with planar electrodes (Fig. 1a), and the seven gas sensors were fabricated accordingly (Fig. 1b). This process was repeated once to confirm that the substrates were completely covered. (3) To remove the organics in excess, the seven sensors were put into quartz boats and gradually heated up to 450 °C for 2 h with a heating rate of 5 °C/min, and then naturally cooled. (4) The annealed sensors were soldered to the testing card of the gas sensing measurement system. Finally, the fabricated gas sensors were aged for more than 24 h by being applied 5 V voltage to enhance their stability and repeatability.

The schematic of the gas sensor and gas sensing measurement system (WS-30A, Weisen, China) are plotted in Fig. 1. As shown in Fig. 1c, the load resistor R_L connected serially with the gas sensor whose resistor is noted as R_S , and the working voltage V_S of the measurement system was 5 V. The different operating temperatures of the gas sensors were adjusted by altering the applied heating voltage (V_h) in the system. The response of the sensor could be obtained by the voltage across R_L , and it was prescribed as follows for reducing gases: $\text{Response} = R_a/R_g$, where R_a was the gas sensor resistance in air and R_g represented the resistance in the target gas.

The response time of the gas sensor was the time required to reach 90% of resistance change during an H_2S exposition,

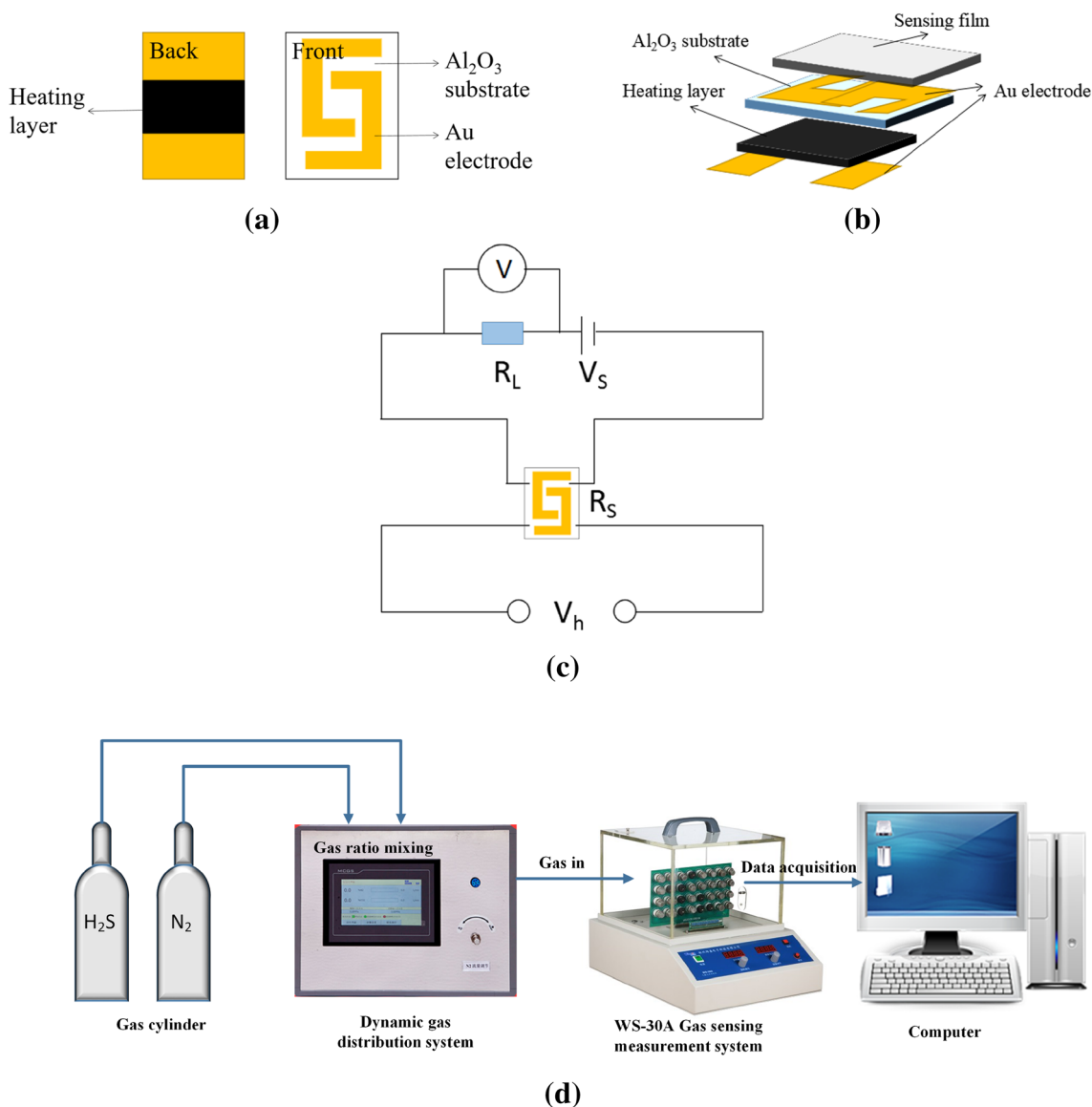


Fig. 1 a Schematic of the planar electrode. b Schematic of the gas sensor. c Measuring electric circuit of gas sensor. d Schematic of gas sensing measurement system

and the recovery time was defined as the time required to reach 90% of resistance change after being exposed to air. Both two values were obtained from the response curves. In the study, as shown in Fig. 1d, the different concentrations of H₂S were firstly obtained by the dynamic gas distribution system connecting with H₂S and N₂ gas cylinders, and N₂ gas was used to adjust the concentration of H₂S gas. And then, the H₂S gases with different concentrations were piped into the chamber of the measurement system. Lastly, the measuring data were collected and processed by computer.

3 Results and discussion

3.1 Characterization

3.1.1 XRD characterization

The crystal structures of the gas sensing materials made from the pure TiO₂, pure α-Fe₂O₃ and 50 mol% α-Fe₂O₃/TiO₂ were characterized by XRD. As shown in Fig. 2a, the XRD pattern of the pure TiO₂ has nine peaks at 2θ = 25.4°, 37.9°, 48.2°, 54.0°, 55.2°, 62.9°, 69.0°, 70.5° and 75.3°, corresponding to (101), (004), (200), (105), (211), (204), (116), (220) and (215) planes of anatase TiO₂ (JCPDS no. 73-1764), respectively, with the lattice constants of a = b = 3.776 Å, c = 9.486 Å. As shown in Fig. 2b, the XRD pattern of the pure α-Fe₂O₃ exhibits eleven characteristic peaks at 2θ = 24.1°, 33.1°, 35.6°, 40.8°, 49.4°, 54.0°, 57.5°, 62.4°, 64.0°, 71.8° and 75.4°, which match with the (012), (104), (110), (113), (024), (116), (122), (214), (300), (1010) and (220) planes of hexagonal hematite (α-Fe₂O₃) (JCPDS no. 24-0072), respectively, with the lattice constants of

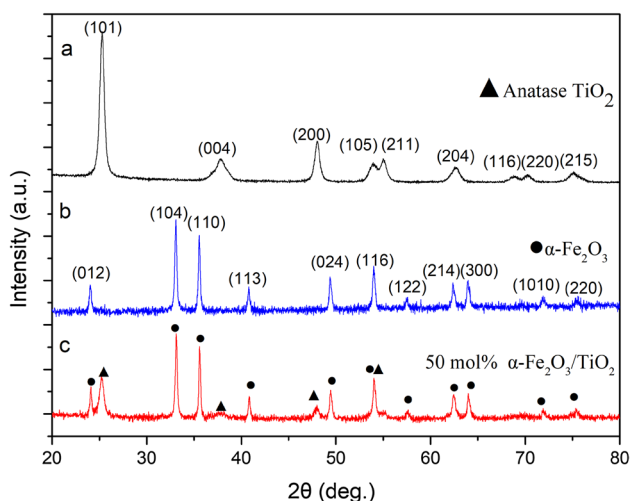


Fig. 2 XRD patterns of gas sensing materials. (a) Anatase TiO₂; (b) α-Fe₂O₃; (c) 50 mol% α-Fe₂O₃/TiO₂

α-Fe₂O₃ are a = b = 5.038 Å, c = 13.772 Å. Notably, the fact that the other phases of iron oxides, such as β-Fe₂O₃, γ-Fe₂O₃, are absent in Fig. 2b, indicates that the phase of the prepared α-Fe₂O₃ is highly pure.

As indicated in Fig. 2c, the XRD pattern of the 50 mol% α-Fe₂O₃/TiO₂ NPs composite displays all the characteristic peaks corresponding to the crystal planes of the anatase TiO₂ and α-Fe₂O₃ at each 2θ. This result also confirms that the prepared composite nanomaterial possesses high purity. In addition, based on the XRD results in Fig. 2, according to the Scherrer Equation, the average crystallite sizes of pure TiO₂, pure α-Fe₂O₃ and 50 mol% α-Fe₂O₃/TiO₂ were calculated as 30 nm, 100 nm, and 50 nm, respectively.

3.1.2 SEM characterization

The SEM images of pure TiO₂, pure α-Fe₂O₃ and 50 mol% α-Fe₂O₃/TiO₂ NPs are presented in Fig. 3, in which all of the NPs demonstrate good dispersibility. As shown in Fig. 3a, the TiO₂ NPs possess a regular and rough-surface morphology with an average size of 50 nm. From Fig. 3b, it can be observed that the average diameter of α-Fe₂O₃ NPs is 100 nm, which is larger than that of the TiO₂ NPs. Figure 3c reveals that, in the composite of α-Fe₂O₃/TiO₂ NPs, both TiO₂ and Fe₂O₃ maintain the same morphologies and dimensions as their pure forms. The size distributions of these NPs in Fig. 3 are basically similar to the results calculated by XRD patterns (Fig. 2).

3.1.3 TEM characterization

To better understand the crystal structure features of the gas sensing materials, the characterization method of TEM was further used. As presented in Fig. 4a, the anatase TiO₂ NPs display a short nanorod-like morphology, which have a distribution of average size 30–50 nm, this result is in agreement with the results obtained from SEM (Fig. 3b). In Fig. 4b, the α-Fe₂O₃ NPs have a distribution of average size 80–120 nm, which is also similar to that from its SEM image (Fig. 3d). As shown in Fig. 4c, the composite of α-Fe₂O₃/TiO₂ is composed of the large α-Fe₂O₃ clusters surrounded by thinner TiO₂ NPs.

To access to the internal structure of the crystal, such as crystal spacing, the HRTEM characterization method was further employed. In the HRTEM images of the pure TiO₂ and α-Fe₂O₃ NPs, as shown in Fig. 5, some well-arranged lattice fringes can be observed. The lattice fringe of TiO₂ displays the spacing of 0.350 nm (Fig. 5a), which conforms to the (101) plane of anatase TiO₂, and the lattice fringes spacing of α-Fe₂O₃ are 0.369 nm and 0.270 nm (Fig. 5b), which match with the (012) and the (104) planes of the hexagonal α-Fe₂O₃, respectively.

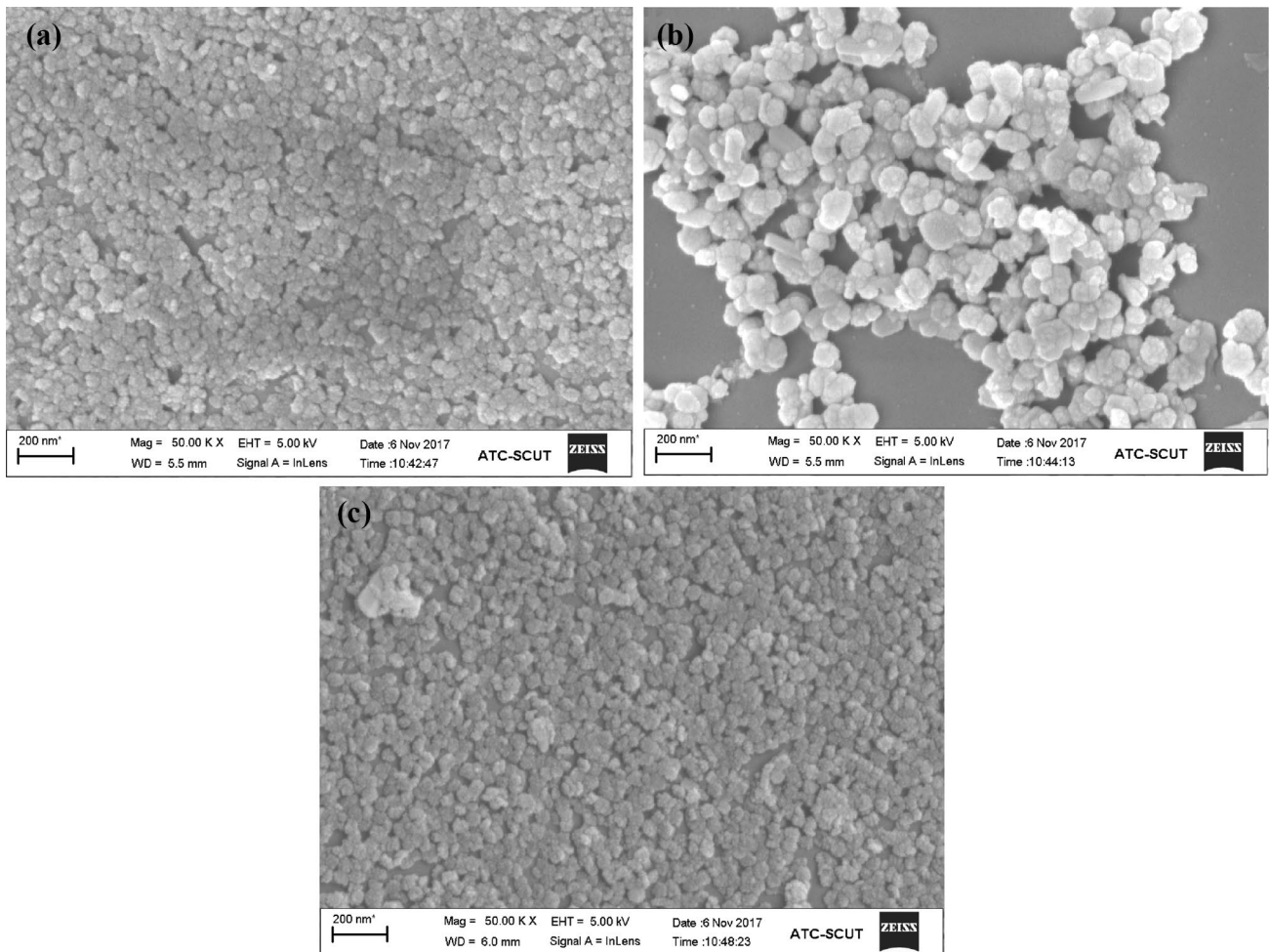


Fig. 3 SEM images of gas sensing materials. **a** Pure TiO_2 NPs; **b** pure $\alpha\text{-Fe}_2\text{O}_3$ NPs; **c** 50 mol% $\alpha\text{-Fe}_2\text{O}_3/\text{TiO}_2$ NPs

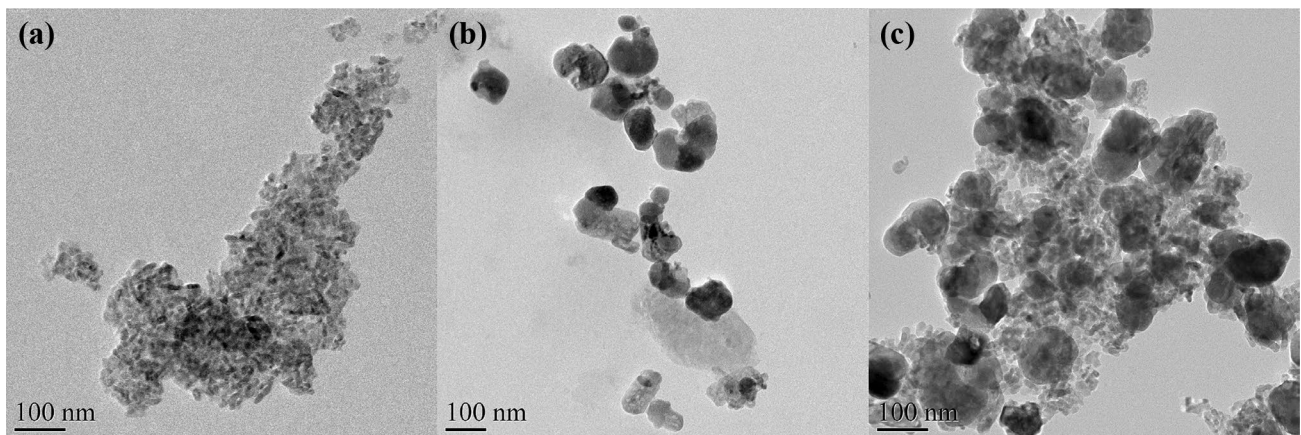


Fig. 4 TEM images of gas sensing materials. **a** Anatase TiO_2 ; **b** $\alpha\text{-Fe}_2\text{O}_3$; **c** 50 mol% $\alpha\text{-Fe}_2\text{O}_3/\text{TiO}_2$

To characterize the composition of the 50 mol% $\alpha\text{-Fe}_2\text{O}_3/\text{TiO}_2$ material, the STEM-EDS mapping method was also applied. As revealed in Fig. 6, in general, the distributions

of Fe, Ti and O elements in $\alpha\text{-Fe}_2\text{O}_3/\text{TiO}_2$ composite material are proved to be uniform. Furthermore, comparing Fig. 6a–d, it can be observed in Fig. 6a that: (i) the iron

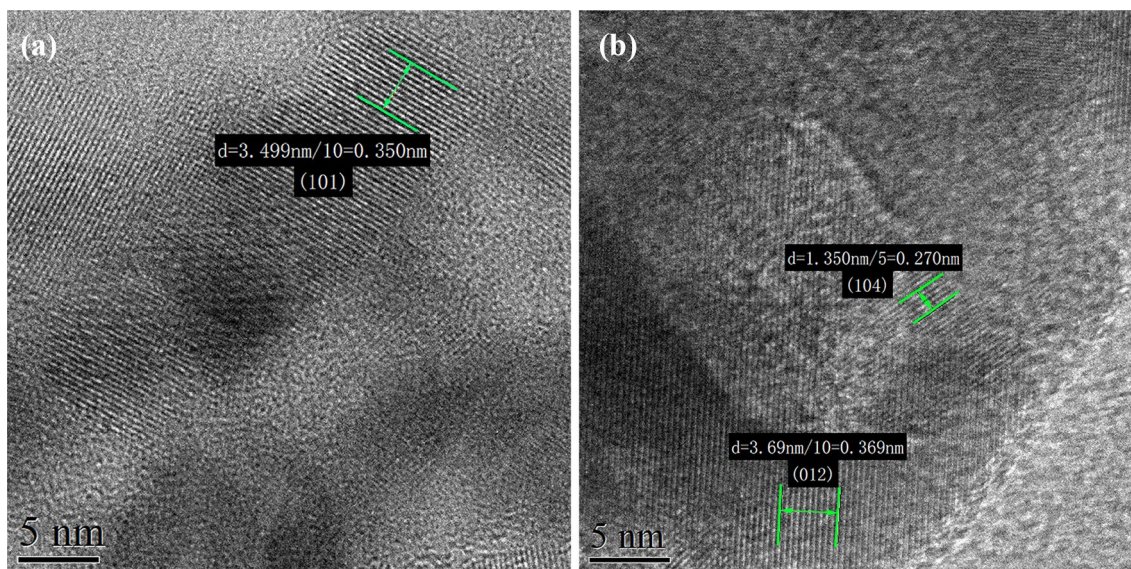


Fig. 5 HRTEM images of two pure gas sensing materials. **a** TiO_2 nanoparticle; **b** $\alpha\text{-Fe}_2\text{O}_3$ nanoparticle

element clusters in the brighter white part, (ii) the titanium element clusters in the darker gray part, and (iii) the distributed morphology of oxygen element in Fig. 6d is similar to that of the $\alpha\text{-Fe}_2\text{O}_3/\text{TiO}_2$ in Fig. 6a, which is in agreement with the results obtained from TEM (Fig. 4c). Therefore, the EDS result demonstrates that, the composite of $\alpha\text{-Fe}_2\text{O}_3/\text{TiO}_2$ is composed of large $\alpha\text{-Fe}_2\text{O}_3$ clusters surrounded by thinner TiO_2 NPs.

3.1.4 XPS characterization

The XPS analysis was used to confirm the compositions of the pure TiO_2 and $\alpha\text{-Fe}_2\text{O}_3/\text{TiO}_2$ NPs, and the obtained XPS spectra are presented in Fig. 7. As shown in Fig. 7a, b, for the pure TiO_2 NPs, in a narrow scan of $\text{TiO}_2\text{-Ti}$ 2p, the two peaks at 458.5 eV and 464.3 eV correspond to the Ti 2p_{3/2} and Ti 2p_{1/2} [29], respectively, with a spin-orbital doublet splitting of 5.8 eV, which reveal that the Ti element is in an oxidation state of +4. Therefore, it matches with the standard spectrum of anatase TiO_2 . In the scanning spectra (Fig. 7c–f) of $\alpha\text{-Fe}_2\text{O}_3/\text{TiO}_2$ composite NPs, a narrow scan of $\alpha\text{-Fe}_2\text{O}_3/\text{TiO}_2\text{-Ti}$ 2p is presented in Fig. 7d, where the two peaks (461.2 eV and 467 eV) correspond to the Ti 2p_{3/2} and Ti 2p_{1/2}, respectively. Figure 7e exhibits a narrow scan of $\alpha\text{-Fe}_2\text{O}_3/\text{TiO}_2\text{-Fe}$ 2p, and the two peaks (713.9 eV and 727.0 eV) correspond to the Fe 2p_{3/2} and Fe 2p_{1/2}, respectively, with a spin-orbital doublet splitting of 13.1 eV, which reveal that the Fe element is in an oxidation state of +3. Therefore, it matches with the Fe_2O_3 spectrum [5, 30]. The peak at 719 eV in Fig. 7e, suggests that the major composition in the Fe_2O_3 NPs is $\alpha\text{-Fe}_2\text{O}_3$. Figure 7f shows the O 1s spectrum of the $\alpha\text{-Fe}_2\text{O}_3/\text{TiO}_2$ NPs, and the O 1s

peaks of $\alpha\text{-Fe}_2\text{O}_3$ and TiO_2 locate at 532.7 eV [31]. The appearance of the shoulder peak at 534.7 eV is probably due to the existence of other oxygen adsorption states, for example, the H–O bonds or the bound oxygen on the material surface [14, 32].

3.2 Gas sensing properties

3.2.1 Optimal operating temperature and doping amount of $\alpha\text{-Fe}_2\text{O}_3$

It has been accepted that, the operating temperature of gas sensor is important for its performance, and a low operating temperature is appropriate for long-term operation due to low power consumption [9]. Therefore, the optimal operating temperature of gas sensor and the doping amount of $\alpha\text{-Fe}_2\text{O}_3$ in the composite material were studied firstly.

According to the procedures described in Sect. 2.4, seven sensors were fabricated with pure TiO_2 , 10, 30, 50, 70, 90 mol% $\alpha\text{-Fe}_2\text{O}_3/\text{TiO}_2$ and pure $\alpha\text{-Fe}_2\text{O}_3$. Being exposed to 50 ppm H_2S , the gas sensing experiments were performed at a series of operating temperatures ranging from room temperature to 450 °C, and the testing results are given in Fig. 8a. Overall, compared with either the pure TiO_2 sensor or the $\alpha\text{-Fe}_2\text{O}_3$ sensor (curves 1 and 7 in Fig. 8a), the 50 mol% $\alpha\text{-Fe}_2\text{O}_3/\text{TiO}_2$ NPs composite sensor enhances the response of gas sensor dramatically.

Obviously in Fig. 8a, the 50 mol% $\alpha\text{-Fe}_2\text{O}_3/\text{TiO}_2$ NPs composite sensor obtained the highest responses at various operating temperatures, where the maximum value 15.6 was achieved at 120 °C, and was 7 times higher than the response of the pure TiO_2 NPs. Moreover, working at the

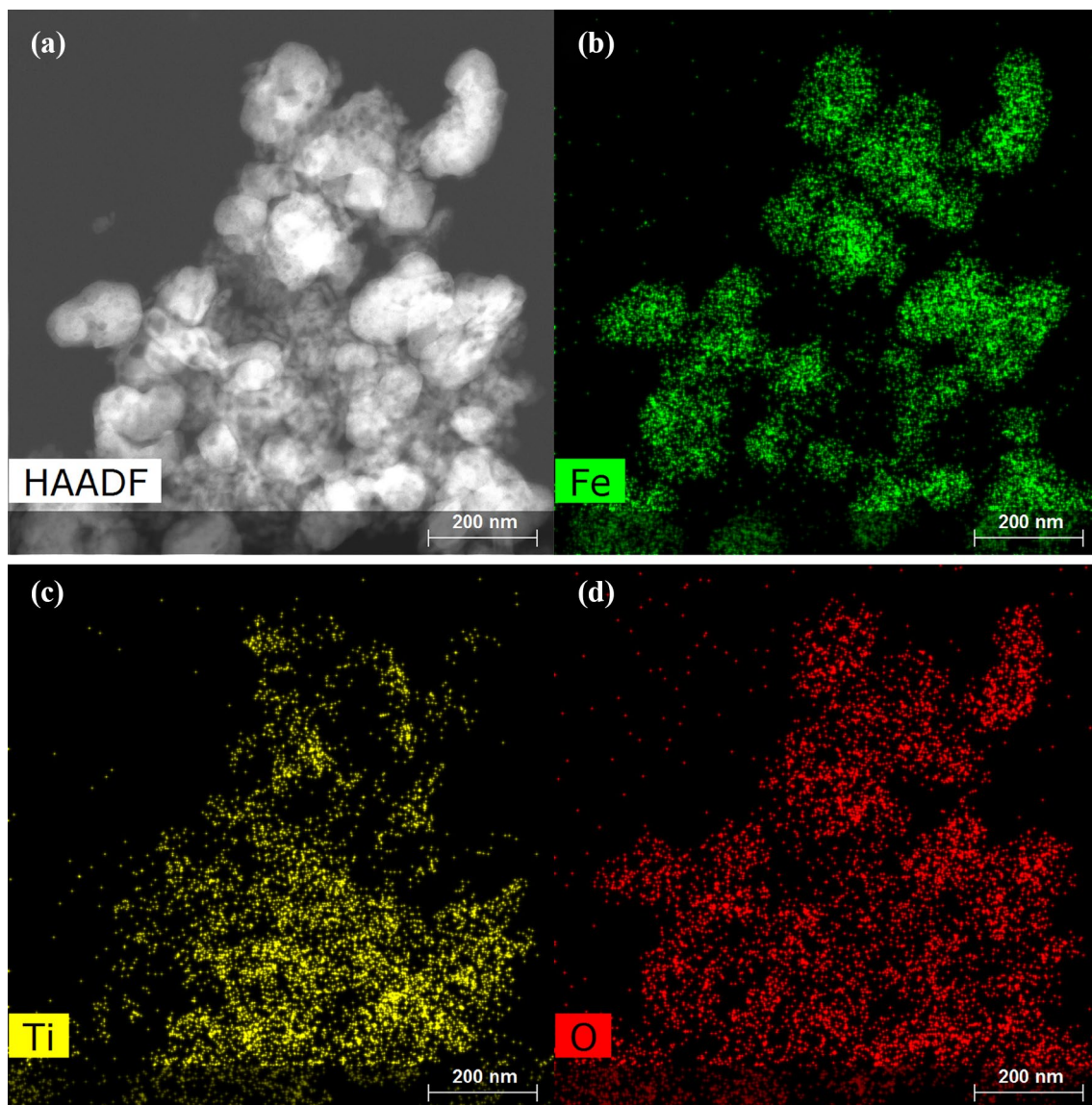


Fig. 6 STEM-EDS mapping result of 50 mol% α -Fe₂O₃/TiO₂ composite gas sensing material. **a** STEM image; **b** elemental distribution of Fe; **c** elemental distribution of Ti; **d** elemental distribution of O

temperature of 120 °C, the effect of different doping molar ratios of α -Fe₂O₃ is plotted in Fig. 8b. It demonstrated that, the responses of the sensors increased to the maximum with the doping amount of α -Fe₂O₃ increasing to 50%, and then decreased. Therefore, the determined optimal conditions maximizing the response were: α -Fe₂O₃ doping amount of 50 mol%, and operating temperature of 120 °C.

The experimental results in Fig. 8 can be analyzed as follows.

(1) When the doping amount of α -Fe₂O₃ is 50 mol%, the largest number of n–n heterostructures can be formed in the α -Fe₂O₃/TiO₂ NPs composite, thus the carriers encountered the largest number of potential barriers in

the transportation process between the grains, eventually lead to the highest initial resistance and resistance variation of the composite in air [33]. However, when the doping amount of α -Fe₂O₃ is further increased higher than 50 mol%, the resistance variation and the responses of the sensors are decreased. Therefore, the response of the 50% mol α -Fe₂O₃/TiO₂ NPs composite sensor to H₂S is the maximum.

(2) When the sensor is operated at the temperatures below 120 °C, the H₂S chemisorption on the sensor surface and the chemical reaction between the adsorbed oxygen species and the adsorbed H₂S molecules are promoted with the rise of operating temperature, which improve the sensor response. Subsequently, under the increased

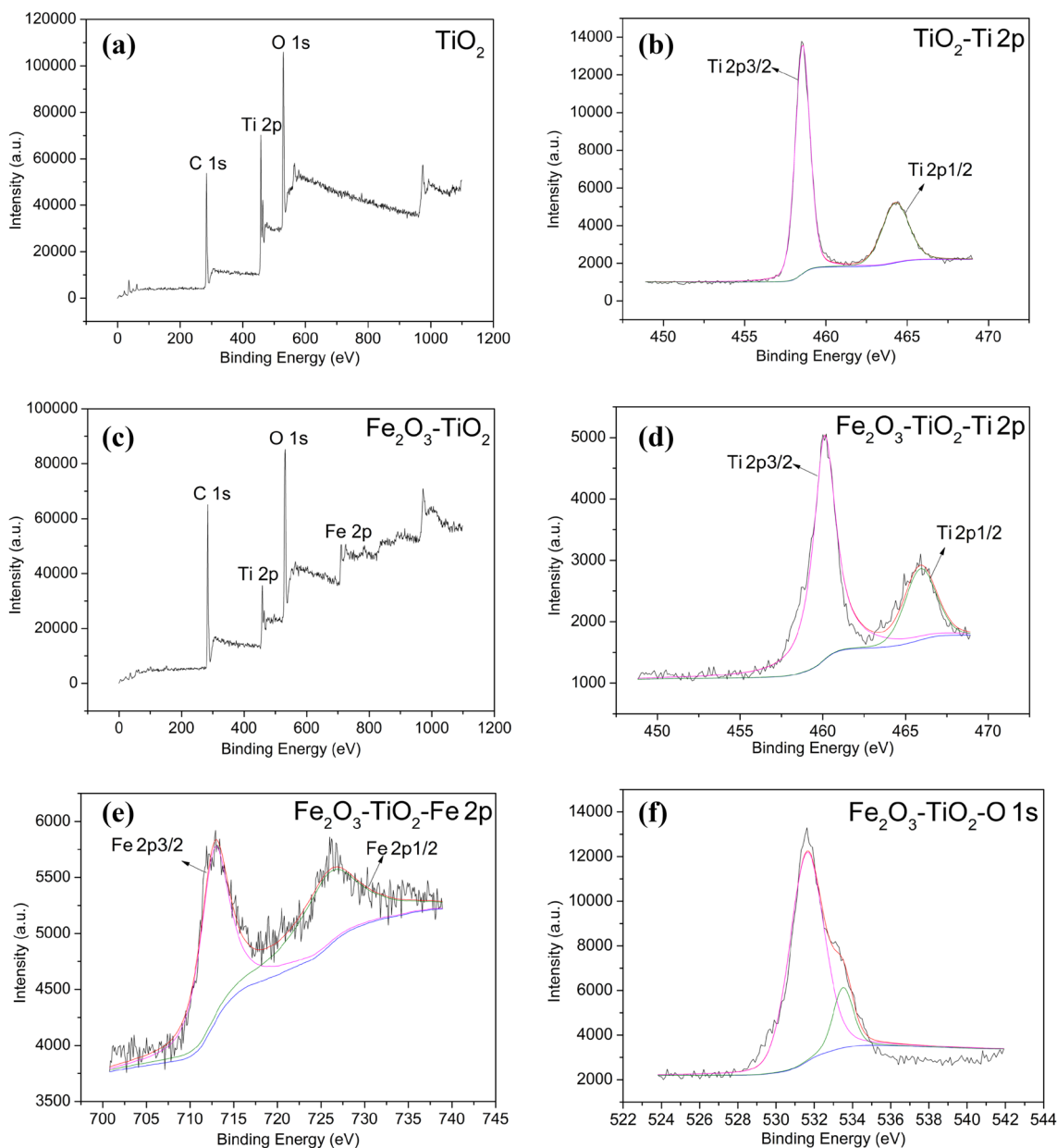


Fig. 7 XPS Spectra of gas sensing materials. Pure TiO_2 NPs: **a** full spectrum diagram; **b** narrow scan of Ti 2p. 50 mol% $\alpha\text{-Fe}_2\text{O}_3/\text{TiO}_2$ NPs: **c** full spectrum diagram; **d** narrow scan of Ti 2p; **e** narrow scan of Fe 2p; **f** narrow scan of O 1s

operating temperature higher than 120°C , the gas sensor response to H_2S decrease inversely, which is probably due to the desorption of H_2S molecules on the sensor surface [1, 34].

Compared with the reported pure TiO_2 gas sensing materials whose operating temperature are often about $200\text{--}300^\circ\text{C}$ [1, 26], in the study, the developed 50 mol% $\alpha\text{-Fe}_2\text{O}_3/\text{TiO}_2$ NPs composite sensor can be effective at a low operating temperature of 120°C , slowing down the aging speed of gas sensor and extending its service life. The

decreased operating temperature from 300 to 120°C can be attributed to the appearance of the large quantity of n–n heterojunctions in the composite, which can reduce the activation energy necessary for gas adsorption, desorption and reaction on the $\alpha\text{-Fe}_2\text{O}_3/\text{TiO}_2$ NPs surface.

3.2.2 Influence of H_2S gas concentration

Figure 9 shows the real-time gas sensing transient responses of the 50 mol% $\alpha\text{-Fe}_2\text{O}_3/\text{TiO}_2$ NPs composite sensor to different concentrations (1–50 ppm) of H_2S at 120°C .

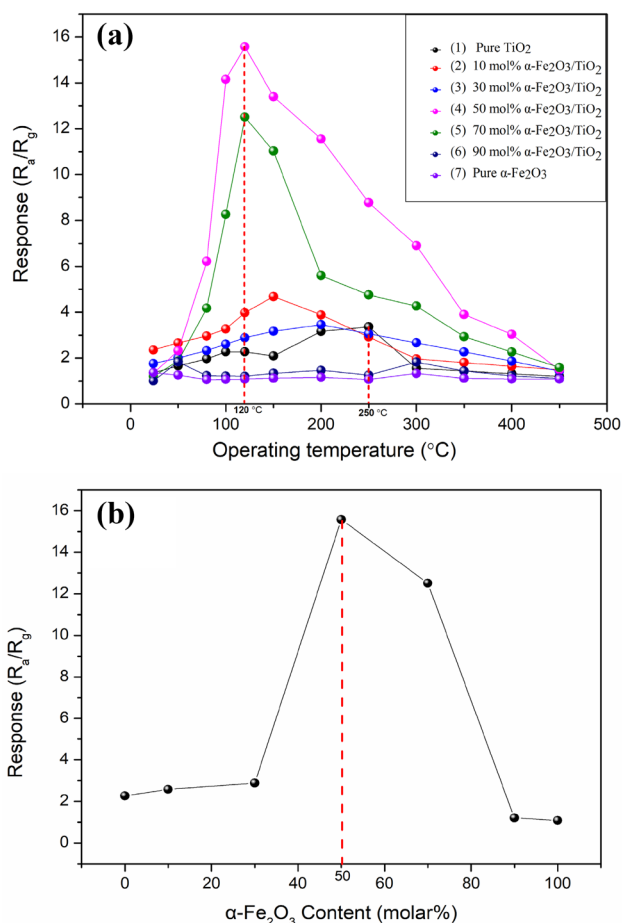
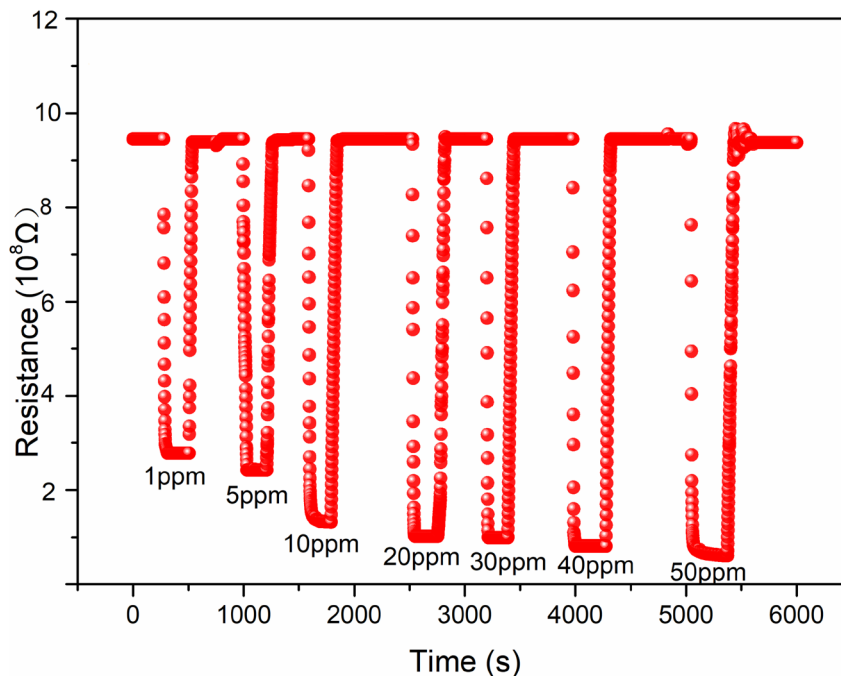


Fig. 8 Responses of the gas sensors to 50 ppm H_2S . **a** Different doping amounts of $\alpha\text{-Fe}_2\text{O}_3$ at various operating temperatures. **b** Effect of different doping amounts of $\alpha\text{-Fe}_2\text{O}_3$ at 120 $^{\circ}\text{C}$

Fig. 9 Real-time gas sensing transient responses of the 50 mol% $\alpha\text{-Fe}_2\text{O}_3/\text{TiO}_2$ NPs composite sensor to different concentrations (1–50 ppm) of H_2S at 120 $^{\circ}\text{C}$



Obviously, the sensor resistance decreased rapidly when the H_2S was piped into the test chamber, and the resistance recovered to its initial value when the H_2S gas was removed and the chamber was refreshed by air, which demonstrated the good reversibility of the gas sensor. The fact that the resistances of the sensor underwent a dramatic decrease when the sensor was exposed to reducing gas (H_2S), indicated that the composite was n-type semiconductor.

Operating at 120 $^{\circ}\text{C}$, the responses of the NPs composite sensor (50 mol% $\alpha\text{-Fe}_2\text{O}_3/\text{TiO}_2$) to the different concentrations (1–50 ppm) of H_2S are plotted in Fig. 10, where the results were calculated by the data in Fig. 9. It displays that, a linear relationship exists between the sensor response and the H_2S concentration. Moreover, it can also be observed that the fabricated 50 mol% $\alpha\text{-Fe}_2\text{O}_3/\text{TiO}_2$ NPs composite sensor is sensitive to the low concentrations (1–10 ppm) of H_2S , whose responses vary between 3.4 and 6.0. From the slope (0.2337) of the regressed relationship between response and H_2S concentration in Fig. 10, it can be reckoned that the change of the response to the variation of H_2S is about 0.2337 ppm^{-1} . Meanwhile, based on the calculation of the limit of detection (LOD): $\text{LOD} = 3\sigma_D/\sigma$ (σ is the slope of the linear part of the calibration curve, σ_D is the standard deviation of the response curve noise in the air), σ_D is about 0.0012. Therefore, it can be estimated that the LOD of the gas sensor to H_2S is as low as 0.015 ppm, indicating that the developed $\alpha\text{-Fe}_2\text{O}_3/\text{TiO}_2$ NPs composite sensor has very low detection limit.

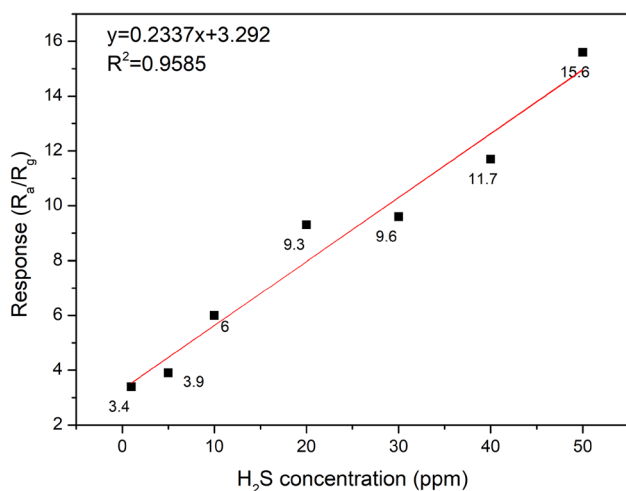


Fig. 10 Response of the 50 mol% α -Fe₂O₃/TiO₂ NPs composite sensor to H₂S with different concentrations (1–50 ppm) at 120 °C

3.2.3 Response and recovery time

The response and recovery time are usually the crucial performance indexes of gas sensor [35]. The real-time gas sensing transient response of the sensor being exposed to 50 ppm H₂S at 120 °C is presented in Fig. 11a, where the response and recovery time were 25 s and 48 s, respectively.

Changing the H₂S concentrations, as shown in Fig. 11b, in the range of 1–50 ppm, the recovery time was basically longer than the response time, and both the response and recovery time were less than 60 s, which was acceptable in the practical gas detection.

3.2.4 Selectivity

Being a crucial property for gas sensor, the gas selectivity was investigated by exposing the sensor to several common toxic gases (H₂S, NH₃, C₂H₅OH, CH₃COCH₃, HCHO, C₆H₆) of 50 ppm at 120 °C, individually. As indicated clearly in Fig. 12, the sensor possessed higher response (15.6) to H₂S than those to other gases, and the response values to NH₃, C₂H₅OH, CH₃COCH₃, HCHO, and C₆H₆ were only 1.1, 1.1, 1.6, 1.4, and 1.5, respectively. Hence, the 50 mol% α -Fe₂O₃/TiO₂ NPs composite sensor exhibited an excellent selectivity to H₂S whose response was more than 10 times higher than those of other tested gases. This experimental result can be explained as follows. The different target gases have different activation energies that are necessary for the gas adsorption, desorption and reaction on the α -Fe₂O₃/TiO₂ NPs surface, which is related to the selectivity of gas sensor. For the 50 mol% α -Fe₂O₃/TiO₂ NPs composite sensor, the necessary activation energy for the adsorption of H₂S at 120 °C is significantly lower than those for other target gases [5]. Besides, H₂S has high chemical reactivity, and the bond

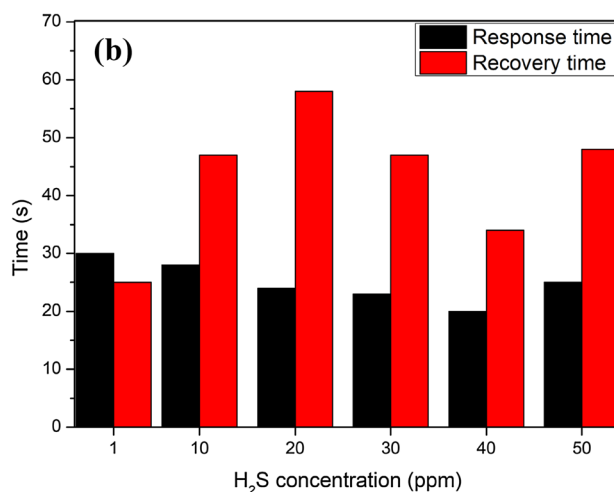
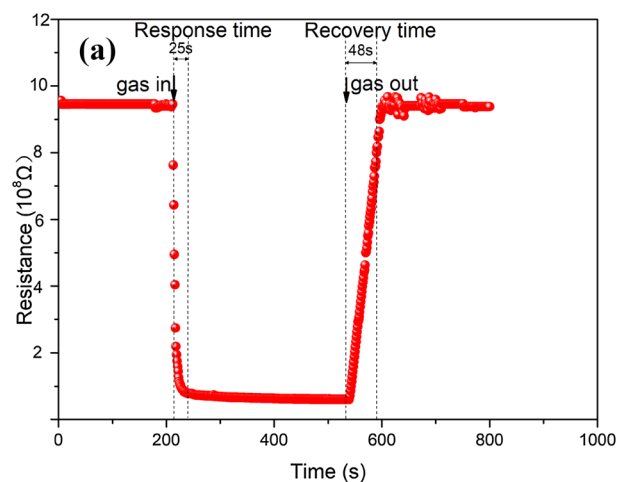


Fig. 11 a Real-time gas sensing transient response of the 50 mol% α -Fe₂O₃/TiO₂ NPs composite sensor to 50 ppm H₂S at 120 °C. **b** Summary of response and recovery time of the 50 mol% α -Fe₂O₃/TiO₂ NPs composite sensor with different H₂S concentrations at 120 °C

energy of H-HS is only 381 kJ/mol, which is the lowest one in the all tested gases [36]. Therefore, H₂S is more likely to react with the gas sensor, and the sensor possessed higher response to H₂S than those to other gases.

3.2.5 Repeatability and stability

Repeating the gas sensing measurements every 5 days during 1 month, the repeatability and stability of the developed 50 mol% α -Fe₂O₃/TiO₂ NPs composite sensor were studied with 50 ppm H₂S at 120 °C. As demonstrated in Fig. 13, with an average error lower than 4.1%, the sensor response remained almost constant around 15.6 during this period, indicating that the sensor had good repeatability and stability.

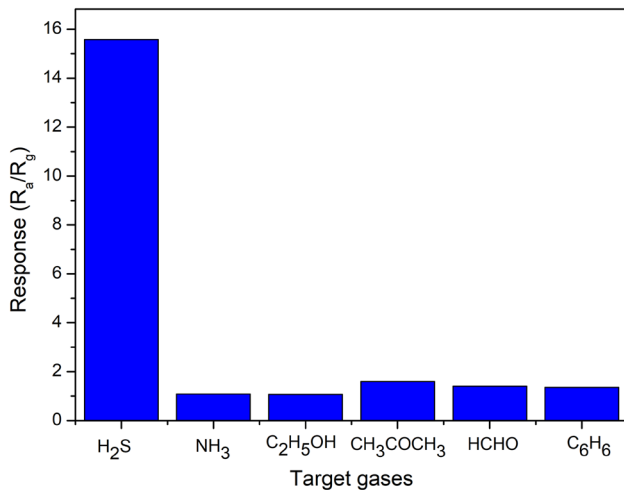


Fig. 12 Selectivity of the 50 mol% α -Fe₂O₃/TiO₂ NPs composite sensor to different target gases of 50 ppm at 120 °C

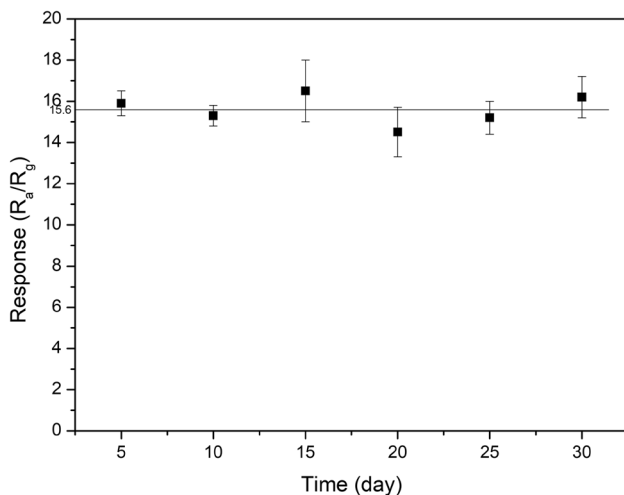


Fig. 13 Repeatability and stability of the 50 mol% α -Fe₂O₃/TiO₂ NPs composite sensor to 50 ppm H₂S at 120 °C in 1 month

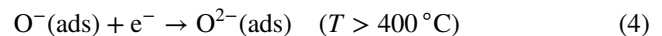
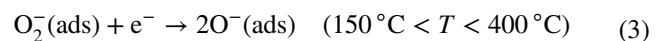
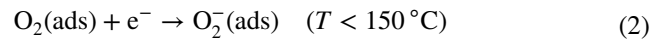
3.3 Gas sensing mechanisms

The gas sensing mechanisms of the α -Fe₂O₃/TiO₂ NPs sensor and its enhanced performance compared with the pure TiO₂ NPs sensor are discussed as follows.

3.3.1 Gas sensing mechanisms of pure TiO₂ NPs gas sensor

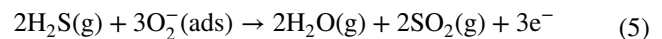
The gas sensing mechanisms of the gas sensor can be explained by the surface-controlled model [37, 38]. The sensor response is determined by the change of material resistance caused by the chemical reaction between the adsorbed oxygen species and the target gas. Besides, the operating temperature can affect the formed type of adsorbed oxygen species, which in turn influence the reactions of the adsorbed

oxygen species with the target gas. In general, O₂⁻ is the dominant oxygen species when the temperature is below 150 °C; the species of O₂⁻ disappears rapidly when the temperature goes up between 150 and 400 °C, O⁻ becomes the dominant oxygen species; when the operating temperature further goes up above 400 °C, O²⁻ is formed. According to these mechanisms, the adsorbed procedures of O₂ on the surface of the materials under different operating temperature may be written in Eqs. (1)–(4) [39, 40]:



In the study, the H₂S gas sensing mechanisms and the energy band diagrams of the pure TiO₂ and α -Fe₂O₃/TiO₂ are schematically shown in Fig. 14.

As shown in Fig. 14a, when the pure TiO₂ was in contact with air, trapping the electrons from the surface of the pure TiO₂, the O₂ molecules in air were adsorbed on the pure TiO₂ surface to form the adsorbed oxygen species with negative charge (O₂⁻ was the dominant oxygen species when the sensor was operated under 120 °C). Thus, the number of electrons on the pure TiO₂ was reduced to form an electron depletion layer, which increased the resistance of the sensor [20]. When the pure TiO₂ was in the presence of H₂S, the O₂⁻ (ads) that had strong oxidability would react rapidly with H₂S. In this process, the trapped electrons on the surface of the materials were released to the conduction band, which resulted in the increasement of the electron density of material. Therefore, the width of electron depletion layer decreased from W₁ to W₂. As a result, with the decreased resistance of the gas sensor, a sharp drop in the resistance of the sensor could be observed in Fig. 11a. The corresponding chemical reaction equation during this process could be written as follows:



3.3.2 Enhanced gas sensing mechanisms of α -Fe₂O₃/TiO₂ NPs composite sensor

Compared with the pure TiO₂ NPs gas sensor, as revealed in Sect. 3.2, the gas sensing properties of α -Fe₂O₃/TiO₂ NPs composite sensor to H₂S have been improved, and the enhanced gas sensing mechanism could be attributed to the following elements:

- (i) Based on the potential barrier modulation and Fermi-level mediated charge transfer effects [5], the electrons in the n–n heterojunction between TiO₂ and α -Fe₂O₃ moved from high energy level (side of TiO₂)

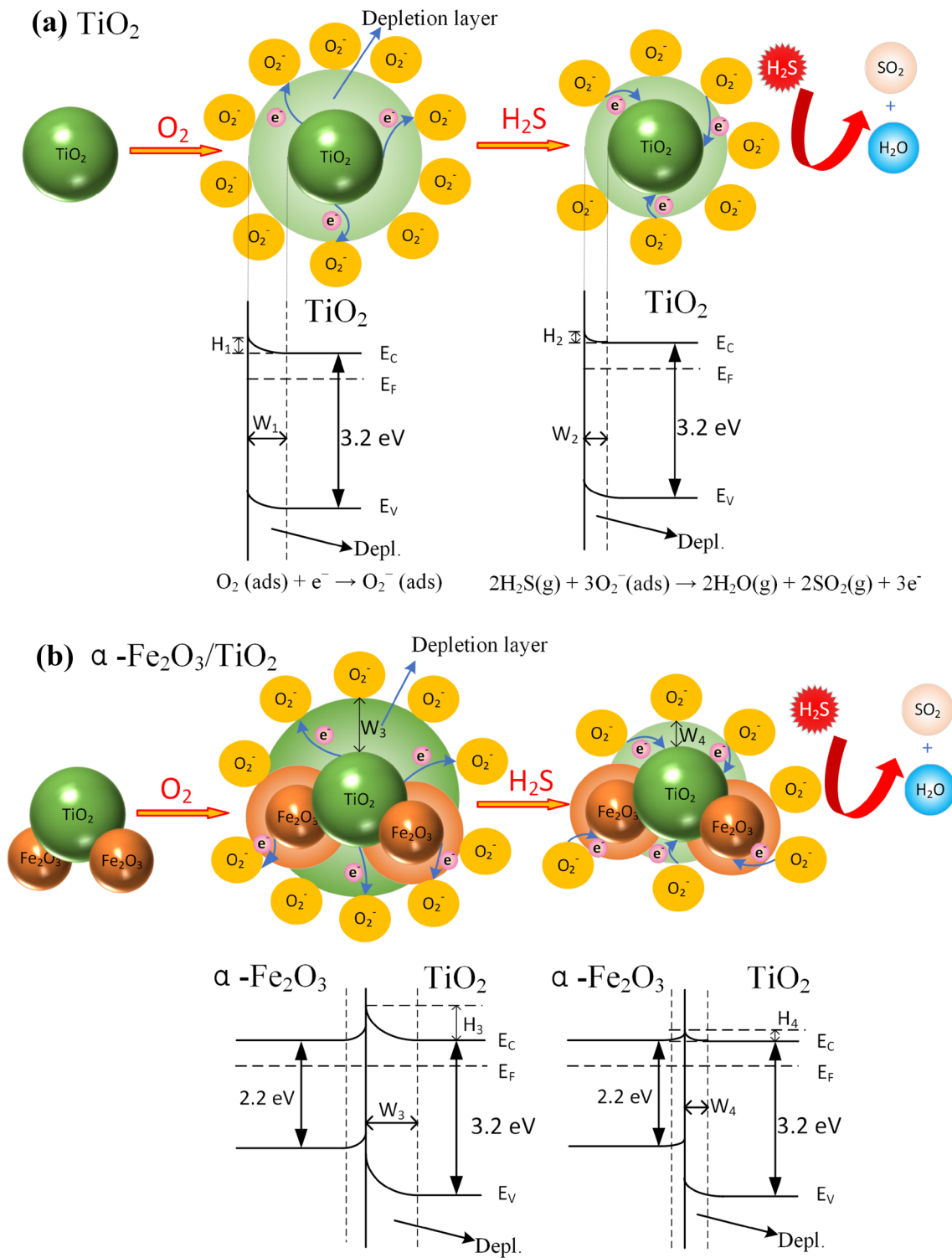


Fig. 14 The H₂S gas sensing mechanisms and energy band diagrams of pure TiO₂ and α -Fe₂O₃/TiO₂

to low energy level (side of α -Fe₂O₃), thereby forming an electron accumulation layer on the low energy level of α -Fe₂O₃ side, rather than the depletion layer. The accumulation layer could be depleted by the

adsorbed oxygen species on the surface of α -Fe₂O₃, as shown in Fig. 14b, so compared with the height H₁ of the pure TiO₂, the height H₃ of the potential barrier at the interface of the composites was increased,

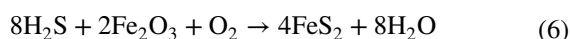
Table 1 Comparison of H₂S sensing properties of different MOS gas sensors

No.	Morphology	Preparation method	Sensor response	Concentration (ppm)	Operating temperature (°C)	Response/recovery time (s)	References
1	α-Fe ₂ O ₃ nanoparticles	Hydrothermal	5.31	10	300	30/5	[9]
2	Cu-doped ZnO	Sol-gel	4.7	50	250	8/250	[48]
3	TiO ₂ nanowires	Hot filament	11	80	140	705/3000	[49]
4	TiO ₂ /SiO ₂	Atomic layer deposition	14	50	250	5/600	[50]
5	CuO-WO ₃ nanowires	Thermal evaporation	6.72	100	300	200/200	[51]
6	Fe ₂ O ₃ thin films	Electron-beam evaporation	4.5	50	250	64/390	[52]
7	α-Fe ₂ O ₃ /TiO ₂ nanoparticles composite	Low synthesis temperature liquid phase	15.6	50	120	25/48	Our work

and accordingly, the initial resistance of the α-Fe₂O₃/TiO₂ NPs composite in air was increased. While being exposed in H₂S, the resistance of the composite was similar to that of pure TiO₂, and the height H₄ of the potential barriers was equal to H₂ of pure TiO₂ [5], thus there existed the larger resistance variation in the H₂S gas, which was beneficial to the enhancement of the sensor response.

In addition, there was also a Fermi-level mediated charge transfer effect between the n-type semiconductors of TiO₂ and α-Fe₂O₃. In the n–n heterojunction, to balance their Fermi levels, the charge transfer was generated, which was an assistance to improve the sensor response [41–43].

- (ii) The forming of the n–n heterojunctions in the α-Fe₂O₃/TiO₂ NPs composite could reduce the width of the conduction channel for the electron transportation, and led to an increase of its initial resistance in air, which improved the sensor response accordingly [44, 45].
- (iii) There existed a synergistic effect between α-Fe₂O₃ and TiO₂. As uncovered in Fig. 8a, compared with either the pure TiO₂ sensor or the α-Fe₂O₃ sensor (curves 1 and 7), the response of the 50 mol% α-Fe₂O₃/TiO₂ NPs composite sensor (curve 4) was enhanced dramatically, which was attributed to the synergistic effect of α-Fe₂O₃ and TiO₂ [46, 47].
- (iv) In addition, according to Ref. [23], the contact of H₂S and α-Fe₂O₃ can also be converted into the metallized FeS₂ by the following chemical reaction:



where the metallized FeS₂ can greatly reduce the material resistance, resulting in higher response.

3.4 Comparison of gas sensors

The properties of our developed α-Fe₂O₃/TiO₂ NPs composite sensor and the other reported H₂S sensors prepared by MOS materials were compared in Table 1, which included the sensor response, operating temperature, and the response/recovery time. Compared with these reported MOS sensors, due to the effects of n–n heterojunctions of two metal oxides, the α-Fe₂O₃/TiO₂ NPs composite sensor had the following advantages: higher response, lower operating temperature, and acceptable shorter response/recovery time in H₂S gas detection. In summary, our developed α-Fe₂O₃/TiO₂ NPs composite sensor achieved good H₂S gas sensing performance under the low operating temperature of 120 °C.

4 Conclusions and perspectives

Based on α-Fe₂O₃/TiO₂ heterojunction NPs composites, operating at low temperature of 120 °C, a high performance of H₂S gas sensor was developed in the study.

The characterization results of the prepared α-Fe₂O₃/TiO₂ NPs composite material with XRD, SEM, TEM, EDS and XPS analysis methods indicated that, (i) TiO₂ was the anatase phase with the average diameter of 50 nm, (ii) the α-Fe₂O₃ NPs had an average diameter of 100 nm, and the composite of α-Fe₂O₃/TiO₂ was composed of large α-Fe₂O₃ clusters surrounded by thinner TiO₂ NPs. The α-Fe₂O₃/TiO₂ NPs composite H₂S gas sensor was characterized in terms of the doping amount of α-Fe₂O₃, operating temperature, response, response/recovery time, selectivity, repeatability and stability. At 120 °C, with the optimal 50 mol% α-Fe₂O₃ doping amount, the developed α-Fe₂O₃/TiO₂ NPs composite

gas sensor demonstrated the following performances: (i) Being exposed to 50 ppm H₂S, its response was 7 times higher than that of the pure TiO₂ NPs. (ii) It achieved the responses of 3.4–15.6 when the sensor was exposed to H₂S of 1–50 ppm. (iii) A linear relationship existed between the sensor response and the H₂S concentration. (iv) Its response/recovery time to 50 ppm H₂S gas were acceptable as 25 s and 48 s, respectively. (v) It exhibited an excellent selectivity to H₂S, whose response to H₂S was more than 10 times higher than those of the other tested gases. (vi) The good repeatability and stability could be observed in 1 month. (vii) Compared with the other reported MOS sensors, the α-Fe₂O₃/TiO₂ NPs composite sensor had superior performances under the temperature of 120 °C. In addition, the mechanism of the improved gas sensing properties was also addressed, where the effects of n–n heterojunctions of two metal oxides were highlighted.

By changing the morphology or crystal phase of TiO₂, or doping with other metal oxides, the enhanced gas sensing mechanisms of metal oxide heterojunction gas sensors can also be applied to develop the other gas sensors to detect different harmful gases. In addition, since humidity may have impact on the performance of the gas sensor, although the operated temperature of the developed α-Fe₂O₃/TiO₂ NPs composite sensor was 120 °C, which was higher than the room temperature, the influence of the humidity will be further studied.

Acknowledgements This work was supported by the Research Funds of the National Natural Science Foundation of Guangdong Province, China [No. 2016A030313478], Science and Technology Program of Guangzhou, China [No. 201904010423], and Open Foundation of State Key Laboratory of Electronic Thin Films and Integrated Devices [KFJJ201803].

Compliance with ethical standards

Conflict of interest There are no conflicts of interest to declare.

References

- X. Tong, W. Shen, X. Chen, J.P. Corriou, *Ceram. Int.* **43**, 14200–14209 (2017). <https://doi.org/10.1016/j.ceramint.2017.07.165>
- S.L. Malone Rubright, L.L. Pearce, J. Peterson, *Nitric Oxide* **71**, 1–13 (2017). <https://doi.org/10.1016/j.niox.2017.09.011>
- X. Tong, W. Shen, X. Chen, J.P. Corriou, *J. Clean. Prod.* **198**, 1066–1075 (2018). <https://doi.org/10.1016/j.jclepro.2018.07.118>
- Y. Liu, J. Parisi, X. Sun, Y. Lei, *J. Mater. Chem. A* **2**, 9919–9943 (2014). <https://doi.org/10.1039/c3ta15008a>
- H. Kheel, G.J. Sun, J.K. Lee, S. Lee, R.P. Dwivedi, C. Lee, *Ceram. Int.* **42**, 18597–18604 (2016). <https://doi.org/10.1016/j.ceramint.2016.08.203>
- S. Zhang, P. Zhang, Y. Wang, Y. Ma, J. Zhong, X. Sun, *A.C.S. Appl. Mater. Interfaces* **6**, 14975–14980 (2014). <https://doi.org/10.1021/am502671s>
- Z. Qu, Y. Fu, B. Yu, P. Deng, L. Xing, X. Xue, *Sens. Actuators B* **222**, 78–86 (2016). <https://doi.org/10.1016/j.snb.2015.08.058>
- Z.S. Hosseini, A. Mortezaali, A. Irajizad, S. Fardindoost, *J. Alloys Compd.* **628**, 222–229 (2015). <https://doi.org/10.1016/j.jallcom.2014.12.163>
- Z. Li, Y. Huang, S. Zhang, W. Chen, Z. Kuang, D. Ao, W. Liu, Y. Fu, *J. Hazard. Mater.* **300**, 167–174 (2015). <https://doi.org/10.1016/j.jhazmat.2015.07.030>
- I. Lee, S.J. Choi, K.M. Park, S.S. Lee, S. Choi, I.D. Kim, C.O. Park, *Sens. Actuators B* **197**, 300–307 (2014). <https://doi.org/10.1016/j.snb.2014.02.043>
- Y. Wang, L. Liu, C. Meng, Y. Zhou, Z. Gao, X. Li, X. Cao, L. Xu, *W. Zhu, Sci. Rep.* **6**, 33092 (2016). <https://doi.org/10.1038/srep33092>
- Y. Seekaew, A. Wisitsoraat, D. Phokharatkul, C. Wongchoosuk, *Sens. Actuators B* **279**, 69–78 (2019). <https://doi.org/10.1016/j.snb.2018.09.095>
- Y. Gönüllü, A.A. Haidry, B. Saruhan, *Sens. Actuators B* **217**, 78–87 (2015). <https://doi.org/10.1016/j.snb.2014.11.065>
- V. Galstyan, E. Comini, C. Baratto, M. Ferroni, N. Poli, G. Faglia, E. Bontempi, M. Brisotto, G. Sberveglieri, *Procedia Eng.* **87**, 176–179 (2014). <https://doi.org/10.1016/j.proeng.2014.11.612>
- P. Chaudhari, S. Mishra, *Measurement* **90**, 468–474 (2016). <https://doi.org/10.1016/j.measurement.2016.05.007>
- F. Pan, H. Lin, H. Zhai, Z. Miao, Y. Zhang, K. Xu, B. Guan, H. Huang, H. Zhang, *Sens. Actuators B* **261**, 451–459 (2018). <https://doi.org/10.1016/j.snb.2018.01.173>
- G. Korotcenkov, B.K. Cho, *Sens. Actuators B* **244**, 182–210 (2017). <https://doi.org/10.1016/j.snb.2016.12.117>
- J.H. Kim, J.H. Lee, A. Mirzaei, H.W. Kim, S.S. Kim, *Sens. Actuators B* **258**, 204–214 (2018). <https://doi.org/10.1016/j.snb.2017.11.063>
- J. Deng, L. Wang, Z. Lou, T. Zhang, *J. Mater. Chem. A* **2**, 9030–9034 (2014). <https://doi.org/10.1039/c4ta00160e>
- C. Cao, C. Hu, W. Shen, *J. Alloys Compd.* **550**, 137–143 (2013). <https://doi.org/10.1016/j.jallcom.2012.09.069>
- Y. Huang, W. Chen, S. Zhang, Z. Kuang, D. Ao, N.R. Alkurd, W. Zhou, W. Liu, W. Shen, Z. Li, *Appl. Surf. Sci.* **351**, 1025–1033 (2015). <https://doi.org/10.1016/j.apsusc.2015.06.053>
- A. Mirzaei, B. Hashemi, K. Janghorban, *J. Mater. Sci. Mater. Electron.* **27**, 3109–3144 (2016). <https://doi.org/10.1007/s10854-015-4200-z>
- A. Mirzaei, S.S. Kim, H.W. Kim, *J. Hazard. Mater.* **357**, 314–331 (2018). <https://doi.org/10.1016/j.jhazmat.2018.06.015>
- A. Mirzaei, K. Janghorban, B. Hashemi, M. Bonyani, S.G. Leonardi, G. Neri, *Ceram. Int.* **42**, 6136–6144 (2016). <https://doi.org/10.1016/j.ceramint.2015.12.176>
- F. Yang, J. Zhu, X. Zou, X. Pang, R. Yang, S. Chen, Y. Fang, T. Shao, X. Luo, L. Zhang, *Ceram. Int.* **44**, 1078–1085 (2018). <https://doi.org/10.1016/j.ceramint.2017.10.052>
- M. Crişan, M. Răileanu, N. Drăgan, D. Crişan, A. Ianculescu, I. Niţoi, P. Oancea, S. Şomăcescu, N. Stănică, B. Vasile, C. Stan, *Appl. Catal. A* **504**, 130–142 (2015). <https://doi.org/10.1016/j.apcata.2014.10.031>
- X. Chen, G. Gu, H. Liu, *Acta Chim. Sin.* **61**, 1592–1596 (2003)
- R. Ambati, P.R. Gogate, *Ultrason. Sonochem.* **40**, 91–100 (2018). <https://doi.org/10.1016/j.ultsonch.2017.07.002>
- X. Yang, H. Fu, L. Zhang, X. An, S. Xiong, X. Jiang, A. Yu, *Sens. Actuators B* **286**, 483–492 (2019). <https://doi.org/10.1016/j.snb.2019.01.096>
- F. Qu, X. Zhou, B. Zhang, S. Zhang, C. Jiang, S. Ruan, M. Yang, *J. Alloys Compd.* **782**, 672–678 (2019). <https://doi.org/10.1016/j.jallcom.2018.12.258>
- N. Jayababu, M. Poloju, M.V. Reddy, *J. Alloys Compd.* **780**, 523–533 (2019). <https://doi.org/10.1016/j.jallcom.2018.11.413>

32. Y. Luo, J. Luo, W. Zhou, J. Mater. Chem. A **1**, 273–281 (2013). <https://doi.org/10.1039/c2ta00064d>
33. J.H. Lee, A. Katoch, S.W. Choi, J.H. Kim, H.W. Kim, S.S. Kim, ACS Appl. Mater. Interfaces. **7**, 3101–3109 (2015). <https://doi.org/10.1021/am5071656>
34. H. Zhang, J. Feng, T. Fei, S. Liu, T. Zhang, Sens. Actuators B **190**, 472–478 (2014). <https://doi.org/10.1016/j.snb.2013.08.067>
35. K. Wetchakun, T. Samerjai, N. Tamaekong, C. Liewhiran, C. Siri Wong, V. Kruefu, A. Wisitsoraat, A. Tuantranont, S. Phaniichphant, Sens. Actuators B **160**, 580–591 (2011). <https://doi.org/10.1016/j.snb.2011.08.032>
36. Z.S. Hosseini, A. Irajizad, A. Mortezaali, Sens. Actuators B **207**, 865–871 (2015). <https://doi.org/10.1016/j.snb.2014.10.085>
37. Z.P. Tshabalala, D.E. Motaung, G.H. Mhlongo, Sens. Actuators B **224**, 841–856 (2016). <https://doi.org/10.1016/j.snb.2015.10.079>
38. L. Liu, X. Li, P.K. Dutta, Sens. Actuators B **185**, 1–9 (2013). <https://doi.org/10.1016/j.snb.2013.04.090>
39. H.J. Kim, J.H. Lee, Sens. Actuators B **192**, 607–627 (2014). <https://doi.org/10.1016/j.snb.2013.11.005>
40. N. Barsan, U. Weimar, J. Electroceram. **7**, 143–167 (2001). <https://doi.org/10.1023/A:1014405811371>
41. W. Tang, J. Wang, Acta Phys. Chim. Sin. **32**, 1087–1104 (2016). <https://doi.org/10.3866/PKU.WHXB201602224>
42. N. Datta, N.S. Ramgir, S. Kumar, Sens. Actuators B **202**, 1270–1280 (2014). <https://doi.org/10.1016/j.snb.2014.06.072>
43. G.J. Sun, S.W. Choi, A. Katoch, J. Mater. Chem. C **1**, 5454 (2013). <https://doi.org/10.1039/c3tc30987h>
44. Y. Lu, Y. Ma, S. Ma, S. Yan, Ceram. Int. **43**, 7508–7515 (2017). <https://doi.org/10.1016/j.ceramint.2017.03.032>
45. J. Ma, Y. Liu, H. Zhang, Sens. Actuators B **216**, 72–79 (2015). <https://doi.org/10.1016/j.snb.2015.04.025>
46. M.M. Arafat, A.S.M.A. Haseeb, S.A. Akbar, Sens. Actuators B **238**, 972–984 (2017). <https://doi.org/10.1016/j.snb.2016.07.135>
47. Y. Liu, L. Wang, H. Wang, Sens. Actuators B **236**, 529–536 (2016). <https://doi.org/10.1016/j.snb.2016.06.037>
48. Amol R. Nimbalkar, Maruti G. Patil, Mater. Sci. Semicond. Proc. **71**, 332–341 (2017). <https://doi.org/10.1016/j.mssp.2017.08.022>
49. M. Munz, M.T. Langridge, K.K. Devarepally, D.C. Cox, P. Patel, N.A. Martin, G. Vargha, V. Stolojan, S. White, R.J. Curry, A.C.S. Appl. Mater. Interfaces **5**, 1197–1205 (2013). <https://doi.org/10.1021/am302655j>
50. F. Yang, J. Zhu, X. Zou, X. Pang, R. Yang, S. Chen, Y. Fang, T. Shao, X. Luo, L. Zhang, Ceram. Int. **44**, 1078–1085 (2018). <https://doi.org/10.1016/j.ceramint.2017.10.052>
51. S. Park, S. Park, J. Jung, T. Hong, S. Lee, H.W. Kim, C. Lee, Ceram. Int. **40**, 11051–11056 (2014). <https://doi.org/10.1016/j.ceramint.2014.03.120>
52. V. Balouria, A. Kumar, S. Samanta, A. Singha, A.K. Debnath, A. Mahajan, R.K. Bedi, D.K. Aswal, S.K. Gupta, Sens. Actuators B **181**, 471–478 (2013). <https://doi.org/10.1016/j.snb.2013.02.013>

Publisher's Note Springer Nature remains neutral with regard to jurisdictional claims in published maps and institutional affiliations.